




# Tensor network study of the spin- $\frac{1}{2}$ Heisenberg antiferromagnet on the shuriken lattice

Philipp Schmoll <sup>1</sup>, Augustine Kshetrimayum,<sup>1,2,3</sup> Jan Naumann <sup>1</sup>, Jens Eisert,<sup>1,2</sup> and Yasir Iqbal <sup>4,\*</sup>

<sup>1</sup>*Dahlem Center for Complex Quantum Systems and Institut für Theoretische Physik, Freie Universität Berlin, Arnimallee 14, 14195 Berlin, Germany*

<sup>2</sup>*Helmholtz-Zentrum Berlin für Materialien und Energie, Hahn-Meitner-Platz 1, 14109 Berlin, Germany*

<sup>3</sup>*Theory Division, Saha Institute of Nuclear Physics, 1/AF Bidhannagar, Kolkata 700 064, India*

<sup>4</sup>*Department of Physics and Quantum Centers in Diamond and Emerging Materials (QuCenDiEM) group, Indian Institute of Technology Madras, Chennai 600036, India*



(Received 6 December 2022; accepted 23 January 2023; published 7 February 2023)

We investigate the ground state of the spin  $S = \frac{1}{2}$  Heisenberg antiferromagnet on the shuriken lattice, also in the presence of an external magnetic field. To this end, we employ two-dimensional tensor network techniques based on infinite projected entangled pair and simplex states considering states with different sizes of the unit cells. We show that a valence bond crystal with resonances over length six loops emerges as the ground state (at any given finite bond dimension) yielding the lowest reported estimate of the ground state energy  $E_0/J = -0.4410 \pm 0.0001$  for this model, estimated in the thermodynamic limit. We also study the model in the presence of an external magnetic field and find the emergence of  $0$ ,  $\frac{1}{3}$ , and  $\frac{2}{3}$  magnetization plateaus. The  $\frac{1}{3}$  and  $\frac{2}{3}$  plateau states respect translation and point group symmetries and feature loop-four plaquette resonances.

DOI: [10.1103/PhysRevB.107.064406](https://doi.org/10.1103/PhysRevB.107.064406)

## I. INTRODUCTION

Systems of antiferromagnetically interacting quantum spins decorated on corner-sharing arrangements of triangles continue to attract much interest as promising platforms for realizing novel quantum phases [1]. Indeed, the arrival of candidate quantum spin liquid materials based on the iconic kagome lattice such as the celebrated herbertsmithite [2–4] and kapellasite [5] have provided an impetus to the field of frustrated magnetism. Their intriguing properties have triggered a flurry of experimental and theoretical studies which established the kagome lattice as a fertile host for a myriad of exotic states. The parameter space of its Heisenberg Hamiltonian in the presence of long-range interactions is host to quantum spin liquids including chiral states, spin and lattice nematics, and valence bond crystals. Recently, a class of materials based on a different corner-sharing arrangement of triangles—the so-called *shuriken lattice* (also called square-kagome, squagome, and squa-kagome lattice)—have come into the limelight as promising candidate *quantum spin liquid materials* [6,7]. No sign of magnetic ordering down to 50 mK has been observed in the spin  $S = \frac{1}{2}$   $\text{Cu}^{2+}$  based materials  $\text{KCu}_6\text{AlBiO}_4(\text{SO}_4)_5\text{Cl}$  [8] and  $\text{Na}_6\text{Cu}_7\text{BiO}_4(\text{PO}_4)_4[\text{Cl}, (\text{OH})_3]$  [9] despite them having large negative Curie-Weiss temperatures of  $-237$  K and  $-212$  K, respectively. This reveals a scenario similar to herbertsmithite for which dominant antiferromagnetic interactions on this highly frustrated lattice prevent the onset of magnetic order. Such studies can be traced back to early work hinting at materials featuring a corner sharing triangu-

lar lattice structure [10]. On the theoretical front, previous investigations into the nature of the ground state of the  $S = \frac{1}{2}$  Heisenberg antiferromagnet have provided compelling evidence for a magnetically disordered ground state while revealing a subtle competition between different types of non-magnetic ground states which remains debated [11–19].

In this work, we employ instances of two-dimensional *tensor network* (TN) algorithms formulated directly in the thermodynamic limit toward resolving the nature of the ground state. Tensor networks are quantum-information-inspired tools that use entanglement as a resource for studying strongly correlated quantum many-body systems [20–23]. They naturally build in quantum correlations and are suited to capture nonlocal entanglement by construction. They do not suffer from the sign problem plaguing quantum Monte Carlo simulations on frustrated systems. Moreover, these techniques can be used to study large system sizes including the thermodynamic limit, thus mitigating finite-size effects. In two spatial dimensions, they are known as *projected entangled pair states* (PEPS) or iPEPS [24,25] in their infinite instance and have become a state-of-the-art numerical tool for studying strongly interacting systems. These techniques have recently proven to be quite successful in studying frustrated model Hamiltonians [26–30], real materials [31–33], open systems [34–39], and nonequilibrium phenomena [40–45].

Recent theoretical works investigating the ground state of the isotropic  $S = \frac{1}{2}$  Heisenberg antiferromagnet on the shuriken lattice have identified two competing *valence bond crystals* (VBCs) involving resonating loops of different lengths: (i) a pinwheel VBC which maximizes the number of smallest possible loops of length four [see Fig. 1(a)] and (ii) a VBC pattern comprising *only* loops of length six [see Fig. 1(b)]. Surprisingly, it has been shown within an effective

\*yiqbal@physics.iitm.ac.in

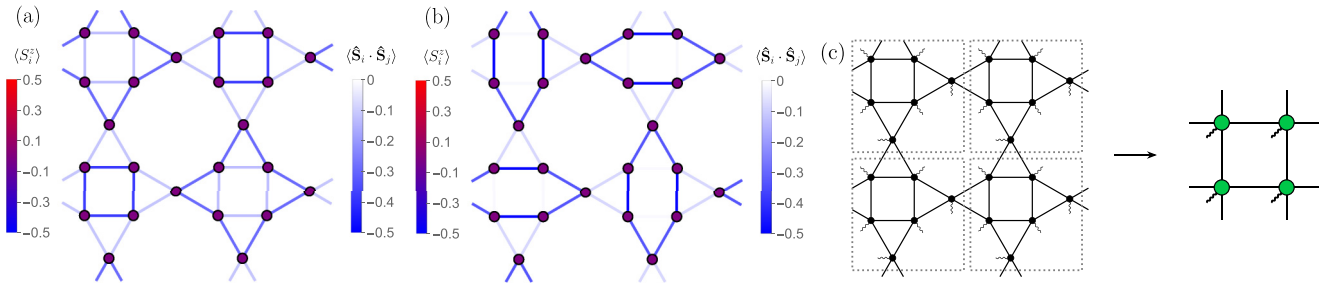


FIG. 1. Nearest-neighbor spin-spin correlations for the ground state configuration of the pinwheel VBC (a) and the loop-six VBC (b) states at  $\chi_B = 12$ . The expectation values of the spin- $z$  component are typically  $<10^{-3}$  and only shown for completeness. (c) Shuriken lattice with spin- $\frac{1}{2}$  degrees of freedom on the sites. The elementary unit cell (gray rectangles) consists of six sites, which are coarse-grained to map the shuriken lattice to a regular square lattice. Straight lines denote virtual bond indices; curly lines denote physical indices in the TN structure.

*resonating valence bond* (RVB) theory that the tunneling processes can be renormalized in such a way that the smallest loops are not always the most relevant in capturing the correct ground state correlations [15]. Indeed, based on a quantum dimer model approach it has been shown in Ref. [15] that the loop-six VBC is more stable energetically compared to the pinwheel VBC when nonlocal processes outside the nearest-neighbor valence bond basis were invoked. Complementing this, based on energetic considerations alone, the pinwheel VBC should conventionally be the expected ground state as found in a recent variational Monte Carlo study [11]. This opens a delicate question on how to properly account for such nonlocal quantum correlations and patterns of long-range entanglement in highly degenerate frustrated systems.

Here, we use a *tensor network* approach to simulate the model directly in the thermodynamic limit. TNs represent the state vector of a many-body system, e.g., reflecting the ground state, as a contraction of a network of local tensors, that are connected by auxiliary indices (bond indices). This enables efficient numerical simulations with only a polynomial scaling in the number of constituents [20,21,23,46]. In this work, we employ the *infinite projected entangled pair state* (iPEPS) [24] and *infinite projected entangled simplex state* (iPESS) (a variant of iPEPS) [47] techniques with an *Ansatz* based on different and specifically tailored unit cell sizes for optimizing the ground state of our model. In this context, the TN is used as an *Ansatz* for the full many-body state vector, consisting of a unit cell of different tensors that generates a translationally invariant state. The accuracy of the *Ansatz* can be systematically improved by increasing the *bond dimension* of the TN, which is the dimension of the virtual indices connecting the local tensors; see Fig. 1(c) (see Appendix). It controls the number of variational parameters in the *Ansatz* and is a measure for the amount of quantum entanglement that can be captured. We mainly employ the so-called simple update [48] to optimize the ground state tensors, which is expected to work well for the gapped model at hand [48–50]. In order to verify its accurate functioning and ability to resolve the close competition between the two candidate ground states, we additionally employ a variational update [51] for this task. The *corner transfer matrix renormalization group* (CTMRG) [52–55] is then used to compute the expectation values of the ground state energy in a variational manner, the spin- $z$  operator as well as the two-point correlations to decipher the nature of the ground state. We also employ additional

$SU(2)$ -symmetric simulations [30,56] for the model. Given the flexibility of the framework, we apply an external magnetic field to study the magnetization process of the model and provide a compelling picture of the nature of phases corresponding to different magnetization plateaus.

## II. MODEL AND METHODS

The model we are considering is the  $S = \frac{1}{2}$  Heisenberg antiferromagnet on the shuriken lattice

$$\hat{H} = \sum_{\langle i,j \rangle} \hat{\mathbf{S}}_i \cdot \hat{\mathbf{S}}_j - h \sum_i \hat{S}_i^z \quad (1)$$

in the presence of an external magnetic field, where  $\hat{\mathbf{S}}_i$  are the  $S = \frac{1}{2}$  operators on site  $i$  and  $\langle i, j \rangle$  denotes nearest neighbors. The shuriken lattice [see Fig. 1(c)] features corner-sharing triangles, and thus leads to only a marginal alleviation of geometric frustration in the presence of antiferromagnetic couplings. Being composed of corner-sharing triangles, it is locally similar to the kagome lattice. At the same time, the shuriken lattice shares two inequivalent sublattices, rendering this lattice ideal to study effects of lattice anisotropy, for which our methods are ideally suited.

We have applied two different TN structures for the simulation of the shuriken lattice. The first *Ansatz* (iPEPS) uses a partial coarse-graining of the shuriken lattice to an irregular square lattice. Inspired by the success for the  $S = \frac{1}{2}$  kagome Heisenberg antiferromagnet [26], the second structure is based on the iPESS *Ansatz* [47] that generalizes iPEPS to lattices with higher simplices. For the shuriken lattice, it is defined on its dual lattice, the so-called  $(4, 8^2)$  Archimedean lattice (also referred to as the square-octagon, Fisher, or CaVO lattice). While the simple update for iPESS incorporates three lattice sites at each update step, it includes six sites for iPEPS (see Appendix). In order to compute expectation values, a unit cell of six sites on the shuriken lattice is coarse-grained into a single tensor on the regular square lattice, as shown in Fig. 1(c). This approach is taken both for the iPESS and the iPEPS simulations, starting from a  $(4, 8^2)$  Archimedean lattice and a partially coarse-grained shuriken lattice, respectively. A directional CTMRG routine then computes effective environment tensors for each coarse-grained iPEPS tensors, such that quantum correlations are fully incorporated when computing expectation values (details are given in the Appendix). This is achieved by a well-chosen environment

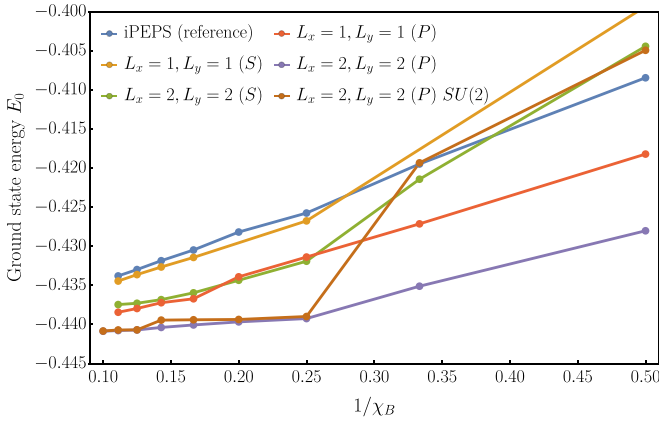


FIG. 2. Ground state energy without magnetic field [ $h = 0$  in Eq. (1)] versus the inverse of the bond dimension  $\chi_B$ . iPESS simulations are denoted by (S), iPEPS simulations by (P).

bond dimension  $\chi_E$ , a refinement parameter controlling the approximations in the CTMRG routine, which is increased until the expectation values converge.

### III. RESULTS ON THE GROUND STATE ENERGY AND DIMER ORDERS

The ground state energy of the shuriken Heisenberg model can be straightforwardly evaluated in the TN representation. The Hamiltonian consists of a sum of nearest-neighbor terms,

$$E_0 = \frac{1}{N} \sum_{\langle i,j \rangle} \langle \psi_0 | h_{i,j} | \psi_0 \rangle, \quad (2)$$

where  $N$  is the number of lattice sites and  $|\psi_0\rangle$  is the normalized ground state vector. The crystallographic unit cell of the shuriken lattice consists of six sites [the dashed regions in Fig. 1(c)]. This *Ansatz*—which imposes translational invariance while being compatible with quantum spin liquid and lattice nematic candidate ground states—would, however, fail to capture translation symmetry broken VBC orders such as the pinwheel and the loop-six VBCs, which are the prime competing ground state candidates. Therefore, we use different unit cell sizes to search for competitive TN *Ansätze* with the lowest ground state energy. The different unit cell configurations are then labeled by the size of the super-unit-cell on the square lattice, denoted by  $(L_x, L_y)$ . A configuration  $(L_x, L_y)$  hence corresponds to an TN state with  $6 \times L_x \times L_y$  spins in total.

In Fig. 2, we show the ground state energy for the iPEPS and iPESS simulations and square lattice unit cells of (1, 1) and (2, 2) as a function of the inverse of the iPEPS bond dimension  $\chi_B$  (bulk bond dimension). Our results are compared to a previous iPEPS study of the model in Ref. [11], using a (1, 1) TN *Ansatz* with a coarse-graining to a honeycomb lattice. Based on our simulations with different sizes of the unit cells, we find the lowest energy is obtained with a (2,2) configuration (unit cell with 24 sites), i.e., corresponding to a valence bond crystal ground state. A similar ground state can be obtained by a (1, 2) configuration in a checkerboard arrangement, which consists of only twelve spins. However, we use the more general state vector *Ansatz* with 24 spins to

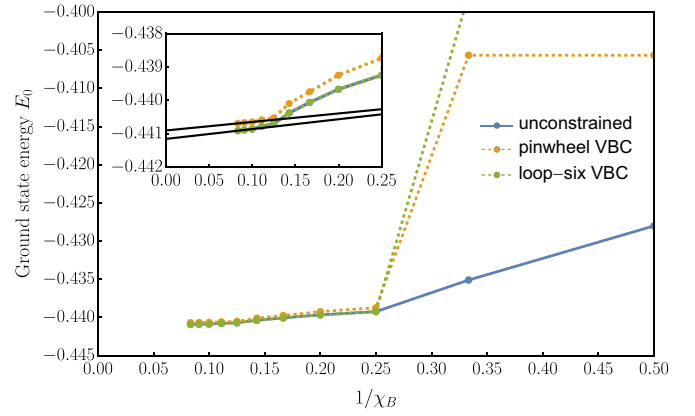


FIG. 3. Comparison of unconstrained and constrained ground state simulations up to  $\chi_B = 12$  for the different configurations imprinted. A first-order polynomial fit is used to extract the infinite bond dimension limit for the three largest bond dimensions.

be able to incorporate possible richer patterns of spin correlations.

In our simulation, the main difference in the iPESS and iPEPS calculations is in the simple update. It is more local in the iPESS with only three sites that are updated at once, compared to six sites in the iPEPS *Ansatz* (see Appendix). This, along with a larger number of variational parameters in the iPEPS *Ansatz*, is responsible for a better ground state approximation with lower energies. For subsequent investigation of the model we therefore use the iPEPS with a (2, 2) unit cell configuration. In addition to the unconstrained simulations, we incorporate fully  $SU(2)$ -symmetric simulations of the model. By imposing the symmetry, the simulated ground state is guaranteed to be in the spin-0 sector, i.e., a spin singlet. In contrast, an unconstrained simulation of the ground state can spontaneously break  $SU(2)$ -symmetry, which would lower its energy. An energy comparison is therefore another way to ascertain the nature of the ground state. For large enough bond dimensions, the  $SU(2)$ -symmetric simulations converge to the same energy as the unconstrained ones, confirming a nonmagnetic VBC ground state with spin-0 of the model as previously reported [11].

Within our iPEPS simulations, we use two ways to ascertain the nature of the VBC ground state: (i) we prepare our initial state with the pinwheel and the loop-six VBC patterns imprinted for a given low bond dimensions and progressively increase  $\chi_B$  in a manner which uses the converged state vectors at any given  $\chi_B$  as initial states for the simulation with one higher bond dimension, and (ii) an unconstrained optimization starting from a random state. In procedure (i) we observe that while both the pinwheel VBC and loop-six VBC patterns remain stable up to  $\chi_B = 12$ , the latter is always lower in energy at any given finite bond dimension (see Fig. 3 and Table I). The resulting spatial spin-spin correlation profiles at  $\chi_B = 12$  are shown in Fig. 1. Further compelling evidence supporting a loop-six VBC ground state scenario for a finite bond dimension is provided by the unconstrained optimization which at higher bond dimensions ( $\chi_B \geq 4$ ) already converges to the energy of the loop-six VBC (see Fig. 3 and Table I). Notice that the pinwheel and loop-six pattern is explicitly

TABLE I. Energy comparison for different ground state configurations of the (2,2) iPEPS. Note that the states at  $\chi_B = [2, 3]$  cannot be used, since the ground state pattern is already imprinted.

$\chi_B$	Unconstrained	Pinwheel	Loop-six
2	-0.428020	-0.405664	-0.397792
3	-0.435105	-0.405664	-0.397792
4	-0.439242	-0.438734	-0.439242
5	-0.439665	-0.439242	-0.439665
6	-0.440058	-0.439738	-0.440058
7	-0.440375	-0.440091	-0.440376
8	-0.440700	-0.440522	-0.440700
9	-0.440776	-0.440584	-0.440776
10	-0.440859	-0.440646	-0.440859
11	-0.440886	-0.440667	-0.440886
12	-0.440908	-0.440689	-0.440908

imprinted in the simulations at  $\chi_B = [2, 3]$ , so that those points are not expressive. The inset of Fig. 3 shows the meaningful, i.e., linear, regime where the energy differences between the two orders are small, highlighting the subtle competition.

An extrapolation to the infinite bond dimension limit using a linear fit of the three values of energy corresponding to the largest  $\chi_B$  yields a lower bound for the energy  $E_l$ . The last data point at  $\chi_B = 12$  provides an upper bound  $E_u$ , such that the true ground state energy lies in the interval  $[E_l, E_u]$  [57]. To estimate the final ground state energy, we compute  $E_0 = (E_u + E_l)/2$  with an error of  $\Delta E = (E_u - E_l)/2$ , which results in

$$\begin{aligned} E_0(\text{pinwheel VBC}) &= -0.4408 \pm 0.0001, \\ E_0(\text{loop-six VBC}) &= -0.4410 \pm 0.0001, \end{aligned} \quad (3)$$

which is lower than previous estimates of the ground state energy [11]. The numerical values for the results in Fig. 3 are summarized in Table I. Given that the estimates of the ground state energy for the pinwheel and loop-six VBC states evaluated in the limit  $\chi_B \rightarrow \infty$  are very close, variational iPEPS simulations have been employed to resolve which of these two competing states wins in this limit. Until the largest reachable bond dimension of  $\chi_B = 7$ , the variational energies lie below the presented simple update energies and reinforce the ground state to be a loop-six VBC [51]. A direct comparison of the simple update and variational energies is presented in Table II.

TABLE II. Energy comparison between simple update and variational energies for the ground state of the loop-six VBC. The variational update uses a two-tensor checkerboard pattern on the coarse-grained shuriken lattice.

$\chi_B$	Simple update	Variational update
2	-0.428020	-0.433600
3	-0.435105	-0.437320
4	-0.439242	-0.439877
5	-0.439665	-0.440162
6	-0.440058	-0.440391
7	-0.440375	-0.440592

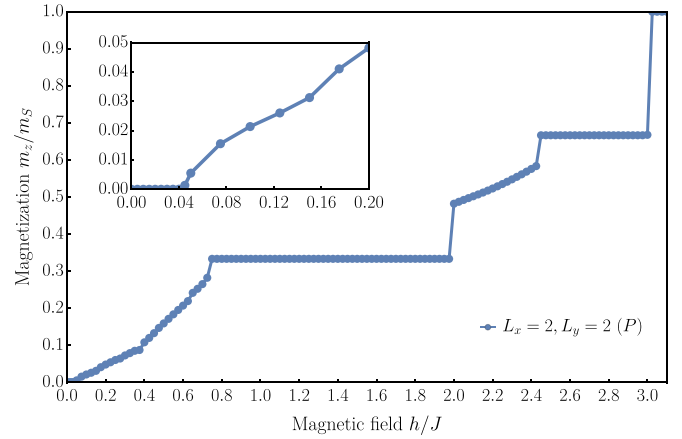


FIG. 4. Magnetization curve of the Heisenberg model for  $\chi_B = 10$ . Upon tuning the magnetic field, two magnetization plateaus at  $\frac{1}{3}$  and  $\frac{2}{3}$  of the saturated magnetization  $m_S = \frac{1}{2}$  appear. Additionally, we find the presence of a small plateau at  $m_z = 0$  indicative of the gapped nature of the ground state.

#### IV. RESULTS ON MAGNETIZATION PLATEAUS

Finally, we study the Heisenberg model on the shuriken lattice in the presence of an external magnetic field. We compute the average magnetization over all the sites in the lattice along the field axis

$$m_z = \frac{1}{N} \sum_i \langle \psi_0(h) | \hat{S}_i^z | \psi_0(h) \rangle, \quad (4)$$

where  $|\psi_0(h)\rangle$  is the normalized ground state vector. In Fig. 4 we show the magnetization curve normalized to the saturation value of  $m_S = \frac{1}{2}$ . The magnetization curve reveals the presence of three magnetization plateaus, at 0,  $\frac{1}{3}$ , and  $\frac{2}{3}$  of the saturation value [17,18,58]. Furthermore, we observe a macroscopic jump from the  $\frac{2}{3}$  plateau to saturation magnetization as conventionally expected due to the presence of a flat one-magnon band which leads to the appearance of localized multimagnon eigenstates [59–64]. The plateau at  $h \rightarrow 0$  is a further indication of the fact that the ground state of the model at  $h = 0$  is actually gapped. An estimate on the size of the spin gap  $\Delta > 0$  is given by the width of the plateau  $\Delta \sim 0.04J$ , consistent with exact diagonalization studies [16,17]. The  $\frac{1}{3}$  and  $\frac{2}{3}$  plateaus can further be characterized by the spatial pattern of spin-spin correlations and the expectation values of the spin- $x$ ,  $-y$ , and  $-z$  components. Those expectation values are shown in Fig. 5 for both phases, at magnetic fields  $h = 1.4$  and  $h = 2.8$ , respectively. Interestingly, one observes that when the magnetic field is turned on, a pattern governed by strong loop-four resonances emerges.

Within error bars in the expectation values, the states at both magnetization plateaus are invariant under translations of the original six-site crystallographic unit cell and also under point group symmetries. It is also visible that correlations are much stronger on the squares compared to the triangle bonds in the lattice. For both plateau states the spins which are not part of the squares are isolated and almost fully polarized (see Fig. 6), implying that they are nearly aligned with the magnetic field. In contrast, the spins on squares, despite a finite

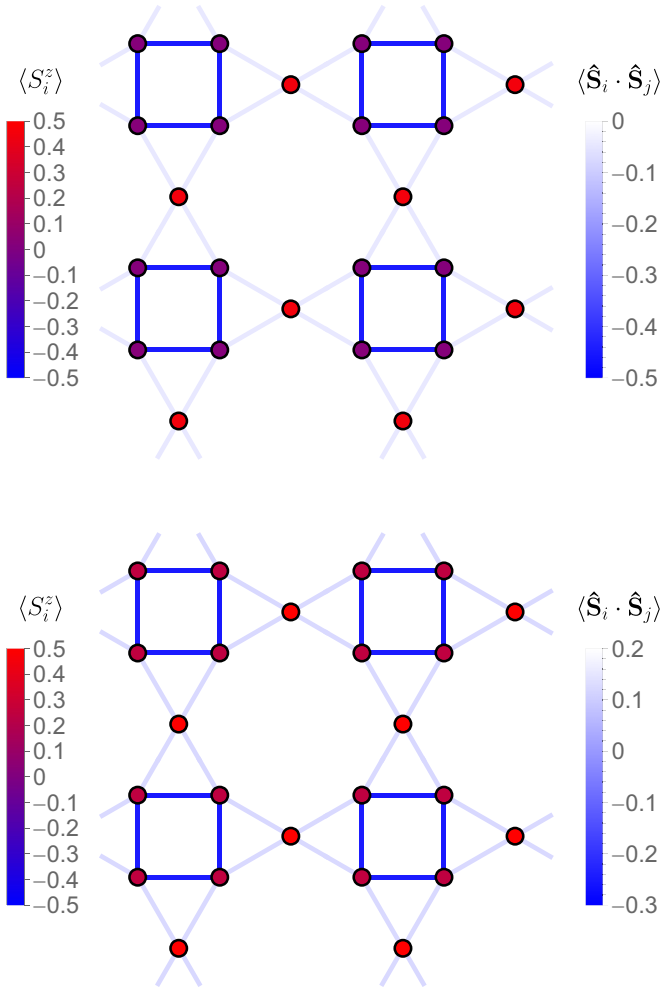


FIG. 5. Ground state configurations of magnetic plateaus for  $h = 1.4$  (top) and  $h = 2.8$  (bottom) at  $\chi_B = 10$ . Both the  $\frac{1}{3}$  plateau state and the  $\frac{2}{3}$  plateau state have strong spin-spin correlations on the squares, whose spins appear to be in an entangled superposition. In contrast, spins on the shuriken sites are isolated and (almost) fully polarized.

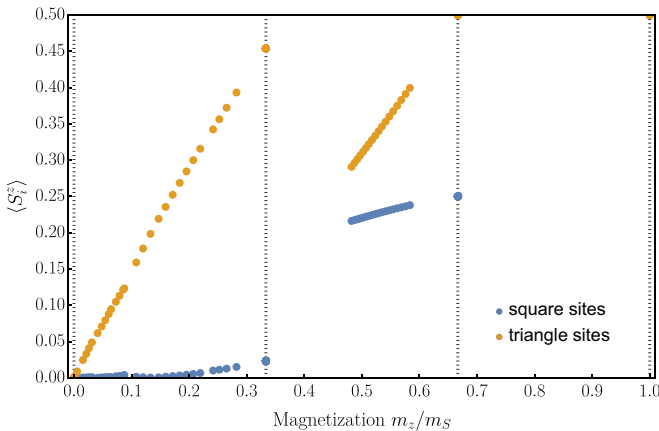


FIG. 6. On-site magnetization of the triangle and square sites versus the magnetic field  $h$ . Dotted vertical lines represent the four magnetization plateaus.

magnetization, possess a nonzero singlet density reminiscent of  $h_z = 0$  resonating plaquettes. This is also evidenced by observing the different magnetization behaviors  $\langle \hat{S}_i^z \rangle$  of the two symmetry inequivalent sites over the range of the magnetization as shown in Fig. 6. The three plateaus appearing in Fig. 4 and the full saturation are shown with dotted lines. The behavior is in good agreement with previous numerical diagonalization studies of the model on finite systems [17].

Following the discussion of an analytic description for the magnetic plateau states of the Heisenberg model on the kagome lattice [65], one can similarly construct the  $\frac{2}{3}$  plateau state on the shuriken lattice. For the  $\frac{2}{3}$  case, one can see in Figs. 5 and 6 that the expectation value  $\langle \hat{S}_i^z \rangle$  is roughly 0.25 for the sites which are part of the square and 0.5 for the sites which are not part of the square. This motivates the conclusion that the state vector for one unit cell consists of an entangled state on the square and a product of this superposition with the fully polarized nonsquare sites as  $|\psi^{2/3}\rangle = |\uparrow\rangle_{\times} |\uparrow\rangle_{\infty}$ . Using this *Ansatz*, it is straightforward to find the ground state vector

$$|\uparrow\rangle_{\times} = \frac{1}{2}(|\downarrow\uparrow\uparrow\uparrow\rangle - |\uparrow\downarrow\uparrow\uparrow\rangle - |\uparrow\uparrow\downarrow\uparrow\rangle + |\uparrow\uparrow\uparrow\downarrow\rangle) \quad (5)$$

for the square terms, consisting of pairwise singlets on the four bonds. Since the individual unit cells are not entangled in our *Ansatz* it is easy to check with exact diagonalization (ED) that the full state is the ground state of the subspace we have chosen. The per-site energy of the analytic construction is  $-2h/6$ . This perfectly fits our simple update results, where for  $h = 2.8$  we find an energy of  $-0.933331$  while the analytic result is  $-0.933333$ . This construction built out of one-magnon states on the squares and fully polarized spins on shuriken sites is the well-known magnon crystal state [18,59,66].

For the  $\frac{1}{3}$  plateau the same approach is not successful. If we limit ourselves to the subspace with fully polarized spins on the nonsquare sites and the superposition on the square sites, we can find a ground state from ED but this time the analytic energy for  $h = 1.4$  of  $-0.566667$  is clearly above the result  $-0.592928$  of the simple update calculations. This is expected however, since as one can see in Fig. 6 the spin expectation values  $\langle \hat{S}_i^z \rangle$  are neither exactly 0.5 for the polarized nor zero for the spins on the square. Therefore, a more sophisticated *Ansatz* would be needed to describe this state, but this is beyond the scope of the current work.

## V. CONCLUSIONS

In this work we have studied the ground state properties of the  $S = \frac{1}{2}$  Heisenberg antiferromagnet on the shuriken lattice using two-dimensional tensor network techniques of iPEPS and iPES. We find that the incorporation of nonlocal correlations proves indispensable in accurately capturing the nature of the ground state, which is shown to be a loop-six VBC at any given finite bond dimension up until  $\chi_B = 12$ . Indeed, here we are faced with a scenario featuring a delicate energetic competition between states governed by different stabilization mechanisms. In particular, we have (i) a pinwheel VBC favored by energy gain from short-range loop resonances and (ii) a loop-six VBC favored by strong resonances over longer-length loops which are amplified by the dressing of virtual

singlets on top of the nearest-neighbor basis. This is precisely what we aim to address by employing the TN framework which naturally contains both these key ingredients and allows us to accurately investigate their interplay to precisely determine the nature of the ground state. Our estimate of the ground state energy per site in the thermodynamic limit obtained by extrapolating  $\chi_B \rightarrow \infty$  is given by  $E_0 = -0.4410 \pm 0.0001$ .

We have also investigated the effect of an external magnetic field in the model and obtained its magnetization curve which shows three magnetization plateaus at  $0$ ,  $\frac{1}{3}$ , and  $\frac{2}{3}$  of the saturation magnetization. The width of the magnetization plateau at zero field gives us an estimate of the spin gap  $\Delta \sim 0.04J$  consistent with exact diagonalization studies [16,17]. The nature of the phases at these plateaus is not only polarized but also shows a strong signature of singlet correlations on four-site plaquettes. These states are found to respect the spatial symmetries (both translation and point group) of the shuriken lattice, in contrast to the pinwheel VBC state.

Our work paves the way for future investigation of the Heisenberg model on the shuriken lattice in more general settings. It would be interesting to study the anisotropic model with different couplings on the square and the triangle bonds, or longer-range couplings which could potentially be of relevance in describing the recently studied materials [6,8,9]. An investigation of the excitation spectrum would be another promising route to reveal the diverse manifestations of frustration [67]. Similarly, the corresponding model for higher spins, e.g.,  $S = 1$ , could be explored, which could be host to a trimerized ground state and display a wealth of magnetization plateaus with exotic phases. This perspective seems even more interesting as it seems plausible to recreate frustrated systems in shuriken lattices under the precisely controlled conditions of *quantum simulations* [68] involving ultracold atoms, giving rise to the interesting situation of benchmarking quantum and classical simulations against each other.

## ACKNOWLEDGMENTS

We thank A. Ralko, R. Thomale, E. Weerden, and H. O. Jeschke for insightful discussions and helpful comments on the manuscript. Y.I. acknowledges support from the Department of Science and Technology (DST), India, through the MATRICS Grant No.

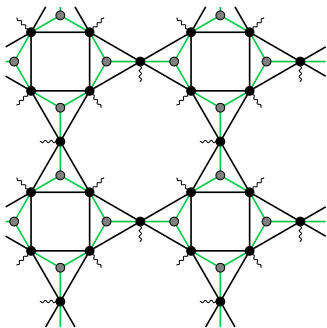


FIG. 7. Shuriken lattice shown in black and its dual lattice [the so-called  $(4, 8^2)$  Archimedean lattice] shown in green. Since the spin- $\frac{1}{2}$ 's live on the links of the dual lattice, additional three-index simplex tensors are introduced on the vertices for the iPESS Ansatz.

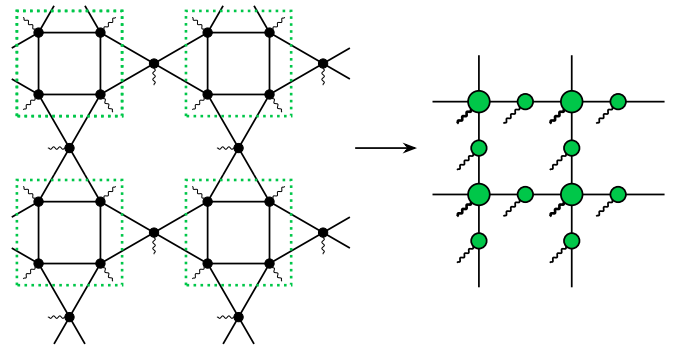


FIG. 8. Shuriken lattice shown on the left and iPEPS Ansatz shown on the right. The four sites on each square are coarse-grained into an effective site, highlighted by the green dotted area. The resulting structure is a square lattice with missing links.

MTR/2019/001042, CEFIPRA Project No. 64T3-1, the ICTP through the Associates Programme, and from the Simons Foundation through Grant No. 284558FY19. This research was supported in part by the National Science Foundation under Grant No. NSF PHY-1748958, IIT Madras through the Institute of Eminence (IoE) program for establishing the QuCenDiEM group (Project No. SB20210813PHMHRD002720), and the International Centre for Theoretical Sciences (ICTS), Bengaluru, India, during a visit for participating in the program “Frustrated Metals and Insulators” (Code: ICTS/frumi2022/9). Y.I. acknowledges the use of the computing resources at HPCE, IIT Madras. The Berlin team has been supported by the BMBF (MUNIQC-ATOMS), the DFG (CRC 183 on “Entangled States of Matter,” Project No. 277101999), and the Helmholtz Center Berlin. The authors would like to thank the HPC Service of ZEDAT, Freie Universität Berlin, for computing time [69].

## APPENDIX: TENSOR NETWORKS

### 1. Tensor network structures and algorithms

In this section, we present further technical details about the tensor network structures and algorithms employed in the main article. We will start with the *infinite projected entangled simplex state* (iPESS) Ansatz [47], which can be straightforwardly extended from the original formulation on the kagome lattice to the shuriken lattice. To this end, we consider the dual lattice [the so-called  $(4, 8^2)$  Archimedean lattice], where the

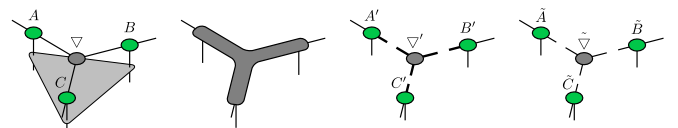


FIG. 9. Simple update in the iPESS simulations of the shuriken lattice. The Trotterized three-body Hamiltonian gate is absorbed into a triangle configuration. A truncated higher-order SVD is used to decompose the resulting six-index tensor back into the separate iPESS tensors. The same procedure is applied to the other simplex tensors along with the different lattice tensors.

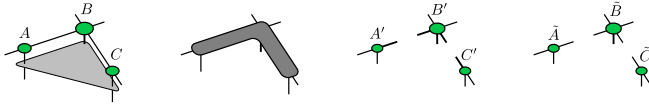


FIG. 10. Simple update in the iPEPS simulations of the shuriken lattice. The Trotterized six-body Hamiltonian gate is absorbed into a bottom-left corner of the deformed square lattice. The individual tensors are restored using two successive SVDs with truncation to a fixed bond dimension. The update of a top-right corner is performed similarly.

spin- $\frac{1}{2}$ 's are located on the lattice links instead of the lattice sites. This lattice is visualized in Fig. 7 in green.

In order to connect the spins, additional purely virtual three-index simplex tensors have to be introduced (shown in gray). An elementary iPESS unit cell therefore consists of six lattice site tensors carrying the physical degree of freedom, and four simplex tensors connecting them.

As an alternative approach we consider a modified version of the *infinite projected entangled pair state* (iPEPS). It is constructed by a partial coarse-graining of the original lattice to a square lattice with missing bonds. To this end we merge the four spins on each square configuration into a single site, which is modeled by a tensor with physical dimension  $p^4$ . The two remaining sites per unit cell are left unchanged. This mapping is shown in Fig. 8.

One advantage that both TN structures share is the fact that one virtual bond in the TN corresponds to only two links in the original shuriken lattice. Since the maximal entanglement shared between neighboring lattice sites is limited by the bond dimension of the TN *Ansatz*, it is favorable to keep this number small. Due to this property, we can directly compare results with the same bond dimension. Note that a coarse-graining of the six spins per unit cell in the shuriken lattice directly results in a regular square lattice.

## 2. Simple update

In order to obtain an approximation of the ground state wave function, we employ the simple update technique [48] in both TNs. This method is based on an imaginary-time evolution under the Hamiltonian [24], in which all the tensors in the networks are updated sequentially. For a sufficiently long evolution, the ground state is projected out. For the iPESS network we employ a regular three-site update of the different simplex configurations [47]. In order to restore the individual tensors after each update, a higher-order singular value decomposition (SVD) is used. During this process, the singular values are truncated to the fixed bulk bond dimension  $\chi_B$  to keep the simulations computationally feasible. The process is

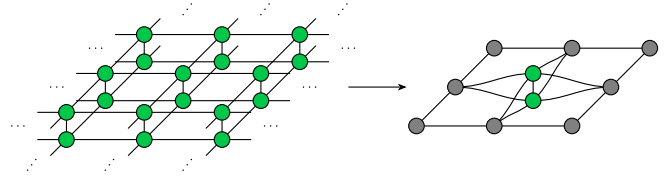


FIG. 11. A CTMRG routine is used to approximate the contraction of the infinite square lattice by a set of fixed-point environment tensors.

illustrated in Fig. 9 for the update of a down simplex, denoted  $\nabla$ , together with the three connected lattice tensors.

The simple update for the iPEPS *Ansatz* on the deformed square lattice follows the same spirit. However, instead of only updating three sites (along with one simplex tensor) as in the iPESS *Ansatz*, we choose a six-site update across corners in the lattice. A single update step is presented in Fig. 10.

Again, the virtual links of the network are kept at a maximal bond dimension  $\chi_B$ , which is achieved by two successive SVDs. Notice that we omit to show additional diagonal tensors carrying the singular values on each virtual link for more clarity in both Fig. 9 and Fig. 10.

Besides the two presented TN approaches, we also implemented a simple update scheme on the original shuriken lattice, using two-body gates on neighboring sites to evolve the wave function. Similarly to the case for the iPESS, the update is very local and could not resolve all the magnetization plateaus present in the model, so that we rejected the simulations.

## 3. Environments and expectation values

In order to accurately compute expectation value for the wave functions obtained by the simple update, we employ a *corner transfer matrix renormalization group* (CTMRG) [52–55] procedure to compute the effective environments. To this end, the six lattice sites per unit cell are coarse-grained into a single iPEPS site with local Hilbert space dimension  $2^6 = 64$ . This maps the shuriken lattice to a regular square lattice, for which a directional CTMRG procedure can directly compute the approximate contraction of the infinite lattice.

As shown in Fig. 11, the contraction of the infinite square lattice is approximated by a set of eight fixed-point tensors surrounding every iPEPS tensor in the unit cell. Expectation values can then be computed straightforwardly by evaluating local operators  $\langle \psi | \hat{O} | \psi \rangle / \langle \psi | \psi \rangle$ , where the environment around the sites on which the operator acts and the norm of the wave function is approximated by the CTMRG tensors.

- [1] L. Savary and L. Balents, Quantum spin liquids: A review, *Rep. Prog. Phys.* **80**, 016502 (2017).  
 [2] P. Mendels, F. Bert, M. A. de Vries, A. Olariu, A. Harrison, F. Duc, J. C. Trombe, J. S. Lord, A. Amato, and C. Baines, Quantum Magnetism in the Paratacamite Family: Towards an Ideal Kagomé Lattice, *Phys. Rev. Lett.* **98**, 077204 (2007).

- [3] T.-H. Han, J. S. Helton, S. Chu, D. G. Nocera, J. A. Rodriguez-Rivera, C. Broholm, and Y. S. Lee, Fractionalized excitations in the spin-liquid state of a kagome-lattice antiferromagnet, *Nature (London)* **492**, 406 (2012).  
 [4] P. Khuntia, M. Velazquez, Q. Barthélemy, F. Bert, E. Kermarrec, A. Legros, B. Bernu, L. Messio, A. Zorko, and

- P. Mendels, Gapless ground state in the archetypal quantum kagome antiferromagnet  $\text{ZnCu}_3(\text{OH})_6\text{Cl}_2$ , *Nat. Phys.* **16**, 469 (2020).
- [5] B. Fåk, E. Kermarrec, L. Messio, B. Bernu, C. Lhuillier, F. Bert, P. Mendels, B. Koteswararao, F. Bouquet, J. Ollivier, A. D. Hillier, A. Amato, R. H. Colman, and A. S. Wills, Kapellasite: A Kagome Quantum Spin Liquid with Competing Interactions, *Phys. Rev. Lett.* **109**, 037208 (2012).
- [6] O. V. Yakubovich, L. V. Shvanskaya, G. V. Kiriukhina, A. S. Volkov, O. V. Dimitrova, and A. N. Vasiliev, Hydrothermal synthesis and a composite crystal structure of  $\text{Na}_6\text{Cu}_7\text{BiO}_4(\text{PO}_4)_4[\text{Cl}(\text{OH})]_3$  as a candidate for quantum spin liquid, *Inorg. Chem.* **60**, 11450 (2021).
- [7] R. Pohle, O. Benton, and L. D. C. Jaubert, Reentrance of disorder in the anisotropic shuriken Ising model, *Phys. Rev. B* **94**, 014429 (2016).
- [8] M. Fujihala, K. Morita, R. Mole, S. Mitsuda, T. Tohyama, S.-i. Yano, D. Yu, S. Sota, T. Kuwai, A. Koda, H. Okabe, H. Lee, S. Itoh, T. Hawaii, T. Masuda, H. Sagayama, A. Matsuo, K. Kindo, S. Ohira-Kawamura, and K. Nakajima, Gapless spin liquid in a square-kagome lattice antiferromagnet, *Nat. Commun.* **11**, 3429 (2020).
- [9] B. Liu, Z. Zeng, A. Xu, Y. Sun, O. Yakubovich, L. Shvanskaya, S. Li, and A. Vasiliev, Low-temperature specific-heat studies on two square-kagome antiferromagnets, *Phys. Rev. B* **105**, 155153 (2022).
- [10] W. P. Wolf, B. Schneider, D. P. Landau, and B. E. Keen, Magnetic and thermal properties of dysprosium aluminum garnet. II. Characteristic parameters of an Ising antiferromagnet, *Phys. Rev. B* **5**, 4472 (1972).
- [11] N. Astrakhantsev, F. Ferrari, N. Niggemann, T. Müller, A. Chauhan, A. Kshetrimayum, P. Ghosh, N. Regnault, R. Thomale, J. Reuther, T. Neupert, and Y. Iqbal, Pinwheel valence bond crystal ground state of the spin- $\frac{1}{2}$  Heisenberg antiferromagnet on the shuriken lattice, *Phys. Rev. B* **104**, L220408 (2021).
- [12] T. Lukan, L. D. C. Jaubert, and A. Ralko, Topological nematic spin liquid on the square kagome lattice, *Phys. Rev. Res.* **1**, 033147 (2019).
- [13] K. Morita and T. Tohyama, Magnetic phase diagrams and magnetization plateaus of the spin-1/2 antiferromagnetic Heisenberg model on a square-kagome lattice with three nonequivalent exchange interactions, *J. Phys. Soc. Jpn.* **87**, 043704 (2018).
- [14] Y. Hasegawa, H. Nakano, and T. Sakai, Metamagnetic jump in the spin- $\frac{1}{2}$  antiferromagnetic Heisenberg model on the square kagome lattice, *Phys. Rev. B* **98**, 014404 (2018).
- [15] A. Ralko and I. Rousochatzakis, Resonating-Valence-Bond Physics Is Not Always Governed by the Shortest Tunneling Loops, *Phys. Rev. Lett.* **115**, 167202 (2015).
- [16] I. Rousochatzakis, R. Moessner, and J. van den Brink, Frustrated magnetism and resonating valence bond physics in two-dimensional kagome-like magnets, *Phys. Rev. B* **88**, 195109 (2013).
- [17] H. Nakano and T. Sakai, The two-dimensional  $S = 1/2$  Heisenberg antiferromagnet on the shuriken lattice: A lattice composed of vertex-sharing triangles, *J. Phys. Soc. Jpn.* **82**, 083709 (2013).
- [18] J. Richter, J. Schulenburg, P. Tomczak, and D. Schmalzfuß, The Heisenberg antiferromagnet on the square-kagome lattice, *Condens. Matter Phys.* **12**, 507 (2009).
- [19] P. Tomczak and J. Richter, Specific heat of the spin- Heisenberg antiferromagnet on squagome lattice, *J. Phys. A: Math. Gen.* **36**, 5399 (2003).
- [20] R. Orús, A practical introduction to tensor networks: Matrix product states and projected entangled pair states, *Ann. Phys.* **349**, 117 (2014).
- [21] J. Eisert, Entanglement and tensor network states, *Model. Simul.* **3**, 520 (2013).
- [22] J. Eisert, M. Cramer, and M. B. Plenio, Area laws for the entanglement entropy, *Rev. Mod. Phys.* **82**, 277 (2010).
- [23] F. Verstraete, J. I. Cirac, and V. Murg, Matrix product states, projected entangled pair states, and variational renormalization group methods for quantum spin systems, *Adv. Phys.* **57**, 143 (2008).
- [24] J. Jordan, R. Orús, G. Vidal, F. Verstraete, and J. I. Cirac, Classical Simulation of Infinite-Size Quantum Lattice Systems in Two Spatial Dimensions, *Phys. Rev. Lett.* **101**, 250602 (2008).
- [25] F. Verstraete and J. I. Cirac, Renormalization algorithms for quantum-many body systems in two and higher dimensions, [arXiv:cond-mat/0407066](https://arxiv.org/abs/cond-mat/0407066).
- [26] H. J. Liao, Z. Y. Xie, J. Chen, Z. Y. Liu, H. D. Xie, R. Z. Huang, B. Normand, and T. Xiang, Gapless Spin-Liquid Ground State in the  $S = 1/2$  Kagome Antiferromagnet, *Phys. Rev. Lett.* **118**, 137202 (2017).
- [27] T. Picot, M. Ziegler, R. Orús, and D. Poilblanc, Spin- $S$  kagome quantum antiferromagnets in a field with tensor networks, *Phys. Rev. B* **93**, 060407(R) (2016).
- [28] T. Picot and D. Poilblanc, Nematic and supernematic phases in kagome quantum antiferromagnets under the influence of a magnetic field, *Phys. Rev. B* **91**, 064415 (2015).
- [29] A. Kshetrimayum, T. Picot, R. Orús, and D. Poilblanc, Spin- $\frac{1}{2}$  kagome XXZ model in a field: Competition between lattice nematic and solid orders, *Phys. Rev. B* **94**, 235146 (2016).
- [30] P. Schmoll and R. Orús, Benchmarking global  $SU(2)$  symmetry in two-dimensional tensor network algorithms, *Phys. Rev. B* **102**, 241101(R) (2020).
- [31] C. Boos, S. P. G. Crone, I. A. Niesen, P. Corboz, K. P. Schmidt, and F. Mila, Competition between intermediate plaquette phases in  $\text{SrCu}_2(\text{BO}_3)_2$  under pressure, *Phys. Rev. B* **100**, 140413(R) (2019).
- [32] A. Kshetrimayum, C. Balz, B. Lake, and J. Eisert, Tensor network investigation of the double layer kagome compound  $\text{Ca}_{10}\text{Cr}_7\text{O}_{28}$ , *Ann. Phys.* **421**, 168292 (2020).
- [33] P. Schmoll, C. Balz, B. Lake, J. Eisert, and A. Kshetrimayum, Finite temperature tensor network algorithm for frustrated two-dimensional quantum materials, [arXiv:2211.00121](https://arxiv.org/abs/2211.00121).
- [34] A. Kshetrimayum, H. Weimer, and R. Orús, A simple tensor network algorithm for two-dimensional steady states, *Nat. Commun.* **8**, 1291 (2017).
- [35] P. Czarnik, L. Cincio, and J. Dziarmaga, Projected entangled pair states at finite temperature: Imaginary time evolution with ancillas, *Phys. Rev. B* **86**, 245101 (2012).
- [36] P. Czarnik and J. Dziarmaga, Variational approach to projected entangled pair states at finite temperature, *Phys. Rev. B* **92**, 035152 (2015).



- [37] P. Czarnik, M. M. Rams, and J. Dziarmaga, Variational tensor network renormalization in imaginary time: Benchmark results in the Hubbard model at finite temperature, *Phys. Rev. B* **94**, 235142 (2016).
- [38] A. Kshetrimayum, M. Rizzi, J. Eisert, and R. Orús, Tensor Network Annealing Algorithm for Two-Dimensional Thermal States, *Phys. Rev. Lett.* **122**, 070502 (2019).
- [39] S. Mondal, A. Kshetrimayum, and T. Mishra, Two-body repulsive bound pairs in a multibody interacting Bose-Hubbard model, *Phys. Rev. A* **102**, 023312 (2020).
- [40] P. Czarnik, J. Dziarmaga, and P. Corboz, Time evolution of an infinite projected entangled pair state: An efficient algorithm, *Phys. Rev. B* **99**, 035115 (2019).
- [41] C. Hubig and J. I. Cirac, Time-dependent study of disordered models with infinite projected entangled pair states, *SciPost Phys.* **6**, 031 (2019).
- [42] A. Kshetrimayum, M. Goihl, and J. Eisert, Time evolution of many-body localized systems in two spatial dimensions, *Phys. Rev. B* **102**, 235132 (2020).
- [43] A. Kshetrimayum, M. Goihl, D. M. Kennes, and J. Eisert, Quantum time crystals with programmable disorder in higher dimensions, *Phys. Rev. B* **103**, 224205 (2021).
- [44] J. Dziarmaga, Time evolution of an infinite projected entangled pair state: Neighborhood tensor update, *Phys. Rev. B* **104**, 094411 (2021).
- [45] J. Dziarmaga, Time evolution of an infinite projected entangled pair state: A gradient tensor update in the tangent space, *Phys. Rev. B* **106**, 014304 (2022).
- [46] J. I. Cirac, D. Pérez-García, N. Schuch, and F. Verstraete, Matrix product states and projected entangled pair states: Concepts, symmetries, theorems, *Rev. Mod. Phys.* **93**, 045003 (2021).
- [47] Z. Y. Xie, J. Chen, J. F. Yu, X. Kong, B. Normand, and T. Xiang, Tensor Renormalization of Quantum Many-Body Systems Using Projected Entangled Simplex States, *Phys. Rev. X* **4**, 011025 (2014).
- [48] H. C. Jiang, Z. Y. Weng, and T. Xiang, Accurate Determination of Tensor Network State of Quantum Lattice Models in Two Dimensions, *Phys. Rev. Lett.* **101**, 090603 (2008).
- [49] P. Corboz, R. Orús, B. Bauer, and G. Vidal, Simulation of strongly correlated fermions in two spatial dimensions with fermionic projected entangled-pair states, *Phys. Rev. B* **81**, 165104 (2010).
- [50] B. Bruognolo, J.-W. Li, J. von Delft, and A. Weichselbaum, A beginner's guide to non-Abelian iPEPS for correlated fermions, *SciPost Phys. Lect. Notes* **25** (2021).
- [51] J. Naumann, E. Weerdenburg, M. Rizzi, J. Eisert, and P. Scholl (unpublished).
- [52] T. Nishino and K. Okunishi, Corner transfer matrix renormalization group method, *J. Phys. Soc. Jpn.* **65**, 891 (1996).
- [53] T. Nishino and K. Okunishi, Corner transfer matrix algorithm for classical renormalization group, *J. Phys. Soc. Jpn.* **66**, 3040 (1997).
- [54] R. Orús and G. Vidal, Simulation of two-dimensional quantum systems on an infinite lattice revisited: Corner transfer matrix for tensor contraction, *Phys. Rev. B* **80**, 094403 (2009).
- [55] R. Orús, Exploring corner transfer matrices and corner tensors for the classical simulation of quantum lattice systems, *Phys. Rev. B* **85**, 205117 (2012).
- [56] P. Scholl, S. Singh, M. Rizzi, and R. Orús, A programming guide for tensor networks with global  $SU(2)$  symmetry, *Ann. Phys.* **419**, 168232 (2020).
- [57] P. Corboz, Improved energy extrapolation with infinite projected entangled-pair states applied to the 2D Hubbard model, *Phys. Rev. B* **93**, 045116 (2016).
- [58] J. Richter, O. Derzhko, and J. Schnack, Thermodynamics of the spin-half square kagome lattice antiferromagnet, *Phys. Rev. B* **105**, 144427 (2022).
- [59] J. Schnack, H. J. Schmidt, J. Richter, and J. Schulenburg, Independent magnon states on magnetic polytopes, *Eur. Phys. J. B* **24**, 475 (2001).
- [60] J. Schulenburg, A. Honecker, J. Schnack, J. Richter, and H.-J. Schmidt, Macroscopic Magnetization Jumps due to Independent Magnons in Frustrated Quantum Spin Lattices, *Phys. Rev. Lett.* **88**, 167207 (2002).
- [61] O. Derzhko and J. Richter, Finite low-temperature entropy of some strongly frustrated quantum spin lattices in the vicinity of the saturation field, *Phys. Rev. B* **70**, 104415 (2004).
- [62] M. E. Zhitomirsky and H. Tsunetsugu, Exact low-temperature behavior of a kagome antiferromagnet at high fields, *Phys. Rev. B* **70**, 100403(R) (2004).
- [63] O. Derzhko, J. Richter, A. Honecker, and H.-J. Schmidt, Universal properties of highly frustrated quantum magnets in strong magnetic fields, *Low Temp. Phys.* **33**, 745 (2007).
- [64] T. Mizoguchi, Y. Kuno, and Y. Hatsugai, Flat band, spin-1 Dirac cone, and Hofstadter diagram in the fermionic square kagome model, *Phys. Rev. B* **104**, 035161 (2021).
- [65] S. Capponi, O. Derzhko, A. Honecker, A. M. Läuchli, and J. Richter, Numerical study of magnetization plateaus in the spin- $\frac{1}{2}$  kagome Heisenberg antiferromagnet, *Phys. Rev. B* **88**, 144416 (2013).
- [66] J. Richter, O. Derzhko, and J. Schulenburg, Magnetic-Field Induced Spin-Peierls Instability in Strongly Frustrated Quantum Spin Lattices, *Phys. Rev. Lett.* **93**, 107206 (2004).
- [67] P. A. McClarty, M. Haque, A. Sen, and J. Richter, Disorder-free localization and many-body quantum scars from magnetic frustration, *Phys. Rev. B* **102**, 224303 (2020).
- [68] A. W. Glaetzle, M. Dalmonte, R. Nath, I. Rousochatzakis, R. Moessner, and P. Zoller, Quantum Spin-Ice and Dimer Models with Rydberg Atoms, *Phys. Rev. X* **4**, 041037 (2014).
- [69] L. Bennett, B. Melchers, and B. Proppe, Curta: A general-purpose high-performance computer at ZEDAT, Freie Universität Berlin, <http://dx.doi.org/10.17169/refubium-26754>.